Journal of the Optical Society of America B
OPTICAL PHYSICS

Deep learning for isolated attosecond pulse reconstruction with the all-optical method

Lihui Meng,[1] Shiqi Liang,[1] Lixin He,[1] Jianchang Hu,[1] Siqi Sun,[1] Pengfei Lan,[1,*] and Peixiang Lu[1,2]

[1]Wuhan National Laboratory for Optoelectronics and School of Physics, Huazhong University of Science and Technology, Wuhan 430074, China
[2]Hubei Key Laboratory of Optical Information and Pattern Recognition, Wuhan Institute of Technology, Wuhan 430205, China
*pengfeilan@hust.edu.cn

Received 2 March 2023; revised 18 August 2023; accepted 18 August 2023; posted 18 August 2023; published 8 September 2023

The characterization of attosecond pulses is crucial for attosecond metrology. In this work, we investigate the isolated attosecond pulse reconstruction with the all-optical method. The results show that this method can characterize isolated attosecond pulses with a duration shorter than 50 attoseconds. Moreover, we develop a deep learning scheme to characterize isolated attosecond pulses. Through supervised learning, the deep neural network learns the mapping from the photon spectrograms to attosecond pulses. It allows complete characterization of the amplitude and phase of isolated attosecond pulses. Compared to the conventional principal component generalized projections algorithm, the reconstruction with our neural network shows superior quality and robustness to noise. Also, the reconstruction computation time is significantly reduced to a few seconds.

https://doi.org/10.1364/JOSAB.489019

1. INTRODUCTION

The generation of attosecond pulses from high-harmonic generation (HHG) [1,2] has allowed the investigation of electron dynamics in atoms, molecules, and condensed matter [3–6]. Nowadays, attosecond light sources can be obtained with a variety of generation schemes, such as HHG with few-cycle laser pulses [7,8], polarization gating (PG) [9–11], double optical gating (DOG) [12], and two-color fields [13–16]. The pulse duration has been progressively reduced. Isolated attosecond pulses of duration as short as 53 attoseconds [17] and 43 attoseconds [18] were experimentally generated by few-cycle driving pulses centered near 1.8 μm.

The characterization of the attosecond pulse is a crucial issue. There are generally two types of attosecond measurement schemes: ex situ and in situ measurements [19]. For ex situ measurement, the position of modulation and diagnosis is different from the position of pulse generation. Reconstruction of attosecond beating by interference of two-photon transitions (RABBIT) [1] and frequency-resolved optical gating (FROG) for complete reconstruction of attosecond bursts (CRAB) (FROG–CRAB) [20] are typically ex situ schemes. In situ measurement modulates attosecond pulses in the same position of the generation. It was first offered for a train of attosecond pulses with an all-optical experimental setup [21]. A weak second-harmonic beam is introduced to gently perturb the generation process. With the different time delays of the two-color field, the attosecond pulse duration can be acquired by reading the modulation of the even harmonic signal. Later on, Kim *et al.* used the noncollinear in situ measurement to characterize isolated attosecond pulses [22]. All-optical FROG for isolated attosecond pulse reconstruction was theoretically and experimentally demonstrated [23]. This in situ scheme enables complete diagnostics of the temporal profile of an isolated attosecond pulse. Recently, the all-optical measurement technique was applied to characterize the attosecond pulses generated from relativistic plasma mirrors [24]. And, an all-optical method for the complete spatio-temporal characterization of isolated attosecond pulses has also been demonstrated [25].

Attosecond pulse reconstruction requires a retrieval algorithm. There are various retrieval algorithms in ex situ measurement schemes, such as the principal component generalized projections algorithm (PCGPA) [26], the least squares generalized projections algorithm (LSGPA) [27], and the ptychographic [28]. As for the in situ scheme, the all-optical FROG also applies the PCGPA to retrieve the temporal profile of an isolated attosecond pulse from the photon spectrogram. However, previous works only demonstrated the reconstruction of pulses with a duration of several hundred attoseconds [22–25]. In this work, we investigate whether it is valid to reconstruct isolated attosecond pulses shorter than 100 attoseconds. Our simulation indicates that the all-optical method works for a sub-100 attosecond pulse. However, when reducing the pulse duration (i.e., increasing the spectral bandwidth), it is difficult to retrieve the sophisticated details of the temporal profile using the conventional PCPG algorithm. Besides, the PCGPA requires massive calculations and thus the retrieval is excessively time-consuming. Therefore, it is necessary to use a

new algorithm to improve the retrieval quality and reduce the computation cost in the all-optical measurement.

A deep neural network (DNN) is a machine learning technique that has been used in various scientific fields. Unlike traditional algorithms, DNNs employs multiple hidden layers to deal with complicated problems. In ultrafast optics, Zahavy *et al*. investigated second-harmonic generation FROG to reconstruct femtosecond pulses based on deep learning [29]. Lately, deep learning has been applied for phase retrieval from dispersion scan traces [30] and attosecond streaking traces [31,32].

In this work, we developed a deep learning scheme to reconstruct isolated attosecond pulses with the all-optical method. Our neural network achieves mapping from the photon spectrograms to pulses via supervised learning. The DNN model only spends a few seconds on the prediction of the pulse profile. It allows the instantaneous reconstruction of isolated attosecond pulses. Compared to the PCGPA, deep learning reconstruction achieves higher precision. Moreover, our simulation results show that our scheme is robust to noise.

2. METHOD AND RESULTS

A. Simulation Model of the All-Optical FROG

The all-optical FROG method is based on the strong-field approximation (SFA) [33]. A Few-cycle driving laser pulse drives HHG in the gas, and the cut-off harmonic supports the generation of an isolated attosecond pulse [34]. Injecting a weak perturbing pulse in the same position modifies the generation process. The high-harmonic spectrum is perturbed and shifted by changing the time delay between the two pulses. The perturbing pulse is too weak to affect the ionization procedure, so it just perturbs the free electron trajectory between the moment of ionization and the moment of re-collision. For an isolated attosecond pulse, we just consider a single trajectory. According to the SFA, the dipole transition matrix element is [21]

$$d^j(t) \propto \langle g|d|e^{-iS_1(t,t'(t),x,p^*)+i\sigma_{p^*}(x,t,t'(t))}\rangle e^{-i\sigma(t,\phi)} + \text{c.c.} \tag{1}$$

Here, the subscript j stands for the corresponding quantum trajectory. S_1 is the unperturbed action, including the effects of the strong field and the ionic core. Ionization starts at the moment t and returns at the moment t', ϕ is the relative phase between the two pulses, and p^* is regarded as an initial moment. The additional phase includes two parts: $\sigma(t,\phi)$ is acquired without the effect of coordinates, and $\sigma_{p^*}(x,t,t'(t))$ is a coordinate-dependent part. $\sigma_{p^*}(x,t,t'(t))$ can be ignored for the weak perturbation. Equation (1) is simplified as

$$\begin{aligned} d^j(t) &= \langle g|d|e^{-iS_1(t,t'(t),x,p^*)}\rangle e^{-i\sigma(t,\phi)} + \text{c.c.} \\ &= d_0^j(t)e^{-i\sigma^j(t,\tau)} + \text{c.c.} \end{aligned} \tag{2}$$

We obtain the additional phase $\sigma(t,\tau) = \int_{t'(t)}^{t} dt'' v_{\text{SFA}}(t'',t)A_s(t'',\tau)$, which is regarded as a gate. τ is the time delay between the two fields. v_{SFA} and $A_s(t'',\tau)$ correspond to the velocity of the unperturbed trajectory and the vector potential of the perturbing field. By changing the time delay, the 2D spectrogram is approximately represented as [23]

$$\begin{aligned} S(\omega,\tau) \propto |a(\omega,\tau)|^2 &= \omega^4|\widetilde{d}(\omega,\tau)|^2 \\ &= \omega^4|\widetilde{d}_0(\omega) \otimes H(\omega,\tau)|^2, \end{aligned} \tag{3}$$

where $\tilde{d}_0(\omega)$ and $H(\omega,\tau)$ correspond to the Fourier transform of $d_0(t)$ and $e^{-i\sigma(\omega,\tau)}$. Equation (3) has the same form as the equation used in the FROG technique. Therefore, the all-optical FROG can employ the PCGPA as the phase retrieval algorithm for a photon spectrogram trace [23].

B. Reconstruction of the Isolated Attosecond Pulses with the PCGPA

Next, we numerically simulate the experimental process of the all-optical scheme. We apply the driving field and the perturbing field for HHG in argon. In our simulation, we add a Gaussian window function on the electric dipole moment to select the short trajectory.

The spectrogram trace is shown in Fig. 1(a). We use the few-cycle pulse centered at 800 nm as the driving field. The intensity is 3×10^{14} W/cm^2. The wavelength and duration of the perturbing field are the same as the driving field. But the intensity is 1×10^{11} W/cm^2. A 161 attosecond pulse is generated by the cutoff harmonic in this condition. Figure 1(b) shows the retrieved trace, which is nearly consistent with the original spectrogram trace. The pulse reconstruction is shown in Fig. 1(c). The retrieved time-domain structure shows a good agreement with the original pulse, including the intensity profile and phase.

To investigate the reconstruction of the sub-100 attosecond pulse, we increase the wavelength of the few-cycle driving fields to generate a broader spectrogram. The wavelength of the driving field and perturbing field is 2000 nm. Other driving laser parameters are the same as Fig. 1. A 96 attoseconds pulse is generated in this condition. As is shown in Fig. 2(a), the photon spectrogram covers a bandwidth of 40 eV and reaches photon energies up to 280 eV. Figure 2(b) is the retrieved spectrogram trace. Figure 2(c) shows that the retrieved pulse agrees well with the original 96 attoseconds pulse.

Furthermore, we increase the wavelength and intensity of the driving fields. The wavelength of the two fields is 3400 nm. The intensity of the driving field is 4.6×10^{14} W/cm^2. The perturbing field's intensity is 1×10^{11} W/cm^2. The ultrabroad spectrogram with a bandwidth of 87 eV is obtained. The duration of the isolated attosecond pulse reduces to 49 attoseconds. Figures 2(d) and 2(e) present the original spectrogram trace and the retrieved spectrogram trace. As shown in Fig. 2(f), the retrieved pulse's central peak and pulse duration agree well with the original pulse, but the small side peaks show obvious disagreements with the original one.

Next, we consider the computation cost of the PCGPA. We define the error as

$$S_{\text{error}} = \left| \sum_x \sum_y S_{\text{org}}[x,y] - \sum_x \sum_y S_{\text{ret}}[x,y] \right|, \tag{4}$$

where $S_{\text{org}}[x,y]$ and $S_{\text{ret}}[x,y]$ correspond to the original trace and the retrieved trace, respectively. x and y are the grid points in horizontal and vertical coordinates. Figure 3 presents the error curve in the reconstruction of the 49 attoseconds pulse. The error drops rapidly in the first 2000 iterations. Then the

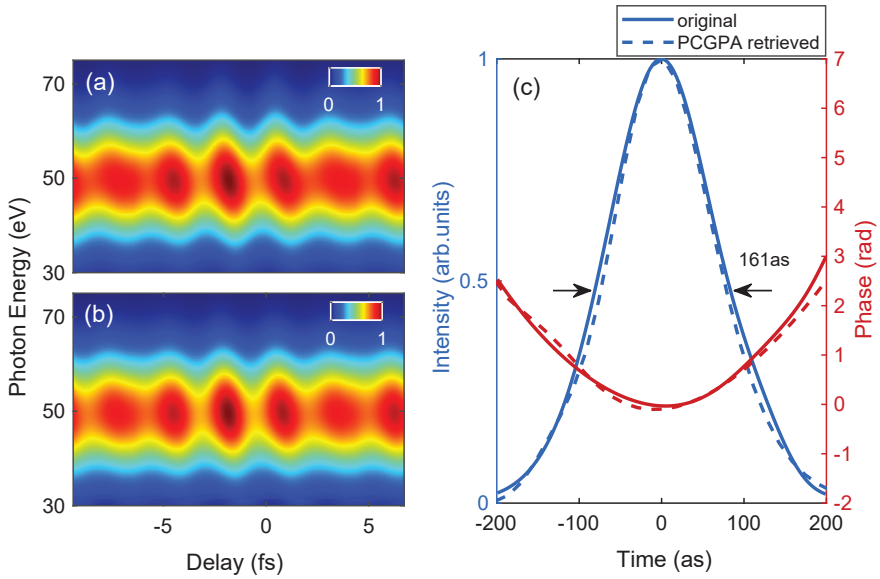

Fig. 1. Reconstruction of the isolated attosecond pulse with the PCGPA. (a) Simulated 2D spectrogram trace. (b) Retrieved trace. (c) Temporal amplitude (blue dashed line) and phase (red dashed line) of the retrieved attosecond pulse from (a), compared to the original pulse (solid lines).

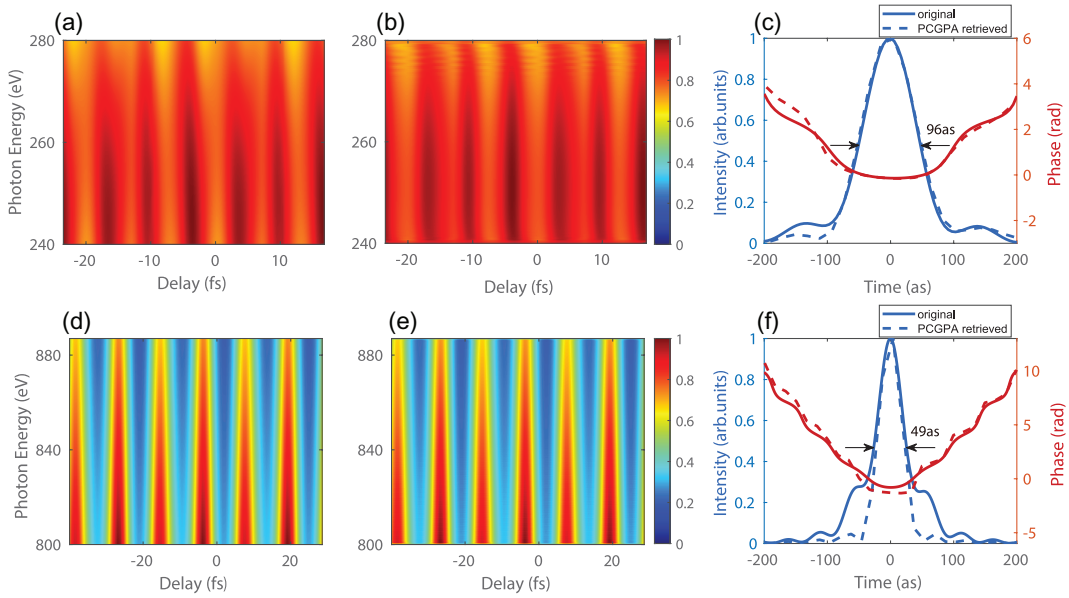

Fig. 2. Reconstruction of sub-100 attoseconds pulse with the PCGPA. (a) Simulated spectrogram trace generated by the few-cycle driving pulse centered at 2000 nm. (b) Retrieved trace from (a). (c) Retrieved pulse (dashed lines) from (a), compared to the original 96 attoseconds pulse (solid lines). (d) Simulated spectrogram trace generated by the few-cycle driving pulse centered at 3400 nm. (e) Retrieved trace from (d). (f) Retrieved pulse (dashed lines) from (a), compared to the original 49 attoseconds pulse (solid lines).

falling rate gradually slows down, and the decline almost stops after 6000 iterations. It means that the PCGP retrieval algorithm requires at least thousands of iterations to complete the reconstruction. On a standard performance computer, the retrieval process for a 96 attoseconds pulse takes a few hours. For the sub-50 attoseconds pulse, the computation cost is more than 10 hours.

C. Deep Learning Retrieval Method

To reduce the computation time, we developed a reconstruction scheme by employing deep learning. Figure 4 depicts the structure of a neural network and training procedure. A neural network architecture contains an input layer, hidden layers, and an output layer. The hidden layers can extract information from the photon spectrograms. Here, the network we used is a convolutional neural network (CNN), and the hidden layers in the CNN consist of many convolutional layers. The convolutional layer is a collection of processing units designed to identify underlying relationships between the input and output [35]. Each unit of the next layer is connected to local patches in the previous layer through a set of weights called a filter bank. In the forward propagation of the neural network, units of the current layer compute a weighted sum of outputs of the previous

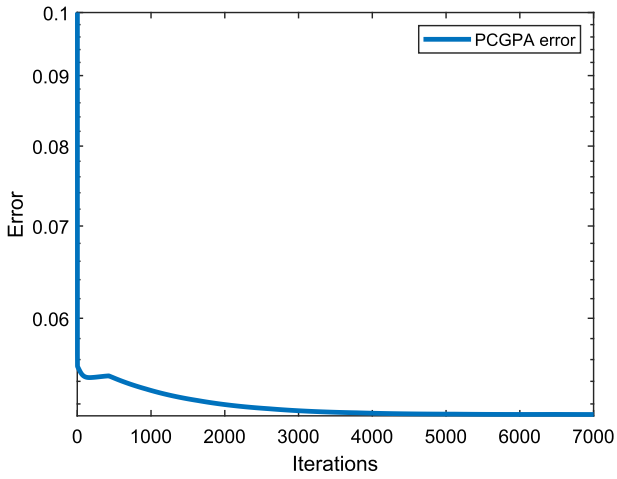

Fig. 3. Error curve of the PCGPA in the reconstruction process of sub-50 attoseconds pulse.

layer. The current layer then employs the nonlinear activation function before passing the results. Training with the datasets, the neural network can learn the feature mapping from the input to the output.

Initially, we generate the datasets by simulating the all-optical measurement. We set a strong driving field and a weak perturbing field in the gas target to generate the 2D photon spectrograms and the attosecond pulses. The spectrograms depend on the laser parameters of the driving fields, e.g., wavelength, intensity, duration, carrier-envelope phase (CEP) and chirp. The chirp of the driving laser is approximately written as a high-order polynomial. Here, we just concentrate on the first three order polynomials. We change these driving laser parameters and randomly smooth the first- to third-order coefficients of the chirp. A huge amount of spectrograms are obtained as a result.

We generated 120,000 spectrograms as the datasets. The datasets are divided into three parts: training set, validation set and test set. Their proportions are, respectively, 80%, 10%, and 10%. Before the training procedure, the dataset must finish pre-processing because the spectrograms' bandwidth covers different photon energies. We externally interpolate blank points to make all the spectrogram traces with a bandwidth of 90 eV. On the time delay axis, we fix the range from −3.5 to 2.5 cycles of driving pulse. After these processes, the pixel number of the dataset image is 100(photon energy) × 100(delay). The spectral step and the time step are 0.9 eV and 0.06 cycles of the driving pulse, respectively. Then, we normalize the spectrograms.

We apply supervised learning to train the network. Here, we employ the temporal profiles of the attosecond pulse as the labels. The pulse can be written as $E(t) = I(t)e^{i\Phi(t)}$. As for the temporal intensity $I(t)$ and phase $\Phi(t)$, label ambiguities exist including the time shift and constant phase shift. To avoid trivial ambiguities in the training process, we first fix the position of the central peak in the time domain to avoid the time shift. The zero-order and first-order terms of the phase have no effect on the shape of the attosecond pulse profile, so we can set them to zero to remove the phase ambiguities. Then we normalize the intensity value. A cost function can measure the discrepancy between the prediction and the supervised output. We set the cost function L as

$$L(y_I, y_\Phi) = w * \left[\frac{\|y_I - \widetilde{y_I}\|}{\|y_I\|} + \eta * \frac{\|y_\Phi - \widetilde{y_\Phi}\|}{\|y_\Phi\|} \right], \tag{5}$$

where y_I and y_Φ represent the normalized intensity value and the absolute phase value. η is a ratio factor of y_Φ, so we can set the value of η to change the weight of the phase in supervised learning. Here, we set $\eta = 1$. By default, every label value innately has an equal effect on the training process. When it comes to pulse reconstruction, the weights of the labels should be chosen according to the temporal pulse structure. Therefore, the weight factor w is defined as

$$w[i] = \begin{cases} = 1 & y_I - y_{\text{th}} > 0, \\ = 0 & y_I - y_{\text{th}} \le 0, \end{cases} \tag{6}$$

where $i = 0, 1, \ldots, N-1$ corresponds to each time point of $E(t)$. The intensity threshold y_{th} is set to be 0.01, allowing the effect of labels to be neglected while the intensity is below the threshold. Through stochastic gradient descent by minimizing the cost function L, the weights of the neural network are optimized. Once the supervised learning is complete, the network model is able to realize the mapping from the photon spectrograms to the isolated attosecond pulses.

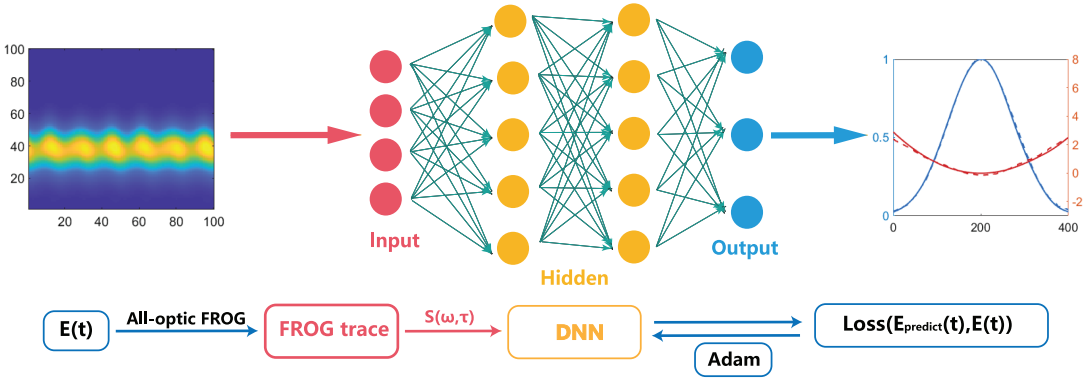

Fig. 4. Network architecture for mapping spectrograms to attosecond pulses and training procedure. A huge amount of spectrogram traces and pulses are generated by simulating the all-optical measurement. We use the traces as datasets and the pulses as labels in supervised learning. The weights in hidden layers can be updated to minimize the loss function via backpropagation. After training, the DNN model can reconstruct isolated attosecond pulses.

In the training procedure, we have attempted to employ three stable CNN architectures: DesNet [36], GoogLeNet Inception-v2 [37], and Xception [38]. After applying the last convolution layer, a flatten layer is used to flatten the multidimensional arrays. We sequentially add several dense layers following the convolution layers. The first few dense layers employ the ReLU activation function, and the last dense layer uses the linear activation function. Among the three network architectures, the Xception architecture has the best appearance. Therefore, we will only display results with the Xception architecture in the following sections.

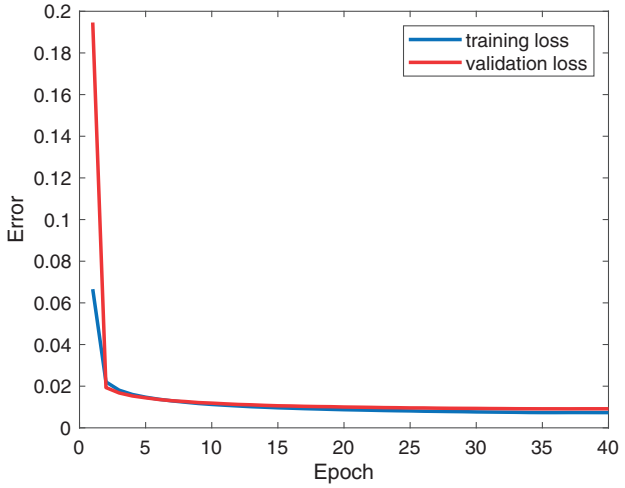

Fig. 5. Loss function evaluated on the training set (blue line) and validation set (red line).

D. Reconstruction of Isolated Attosecond Pulses with Deep Learning Method

We initially considered the time cost of the training. The loss drop curve is shown in Fig. 5. Both the training loss and the validation loss rapidly drop in the first five epochs. Then they slow down and tend to stop dropping after 30 epochs. The validation loss is higher than the training loss after five epochs. Both of them are reduced to below 0.01 after about 30 epochs. The training procedure just lasts less than two hours.

To compare to the retrieval quality of the PCGPA, we also use the DNN model to retrieve pulses from the three spectrograms above. Figures 6(a), 6(c), and 6(e) present the original spectrogram traces. The DNN model spends a few seconds on pulse prediction. The retrieved attosecond pulses are shown in Figs. 6(b), 6(d), and 6(f). The results show that the DNN reconstruction of the isolated attosecond pulses agrees better with the original pulses, including the 49 attoseconds pulse. Concentrating on the sophisticated details of the temporal profile, the DNN model precisely recovers the shape of the side peaks, as shown in Fig. 6(f).

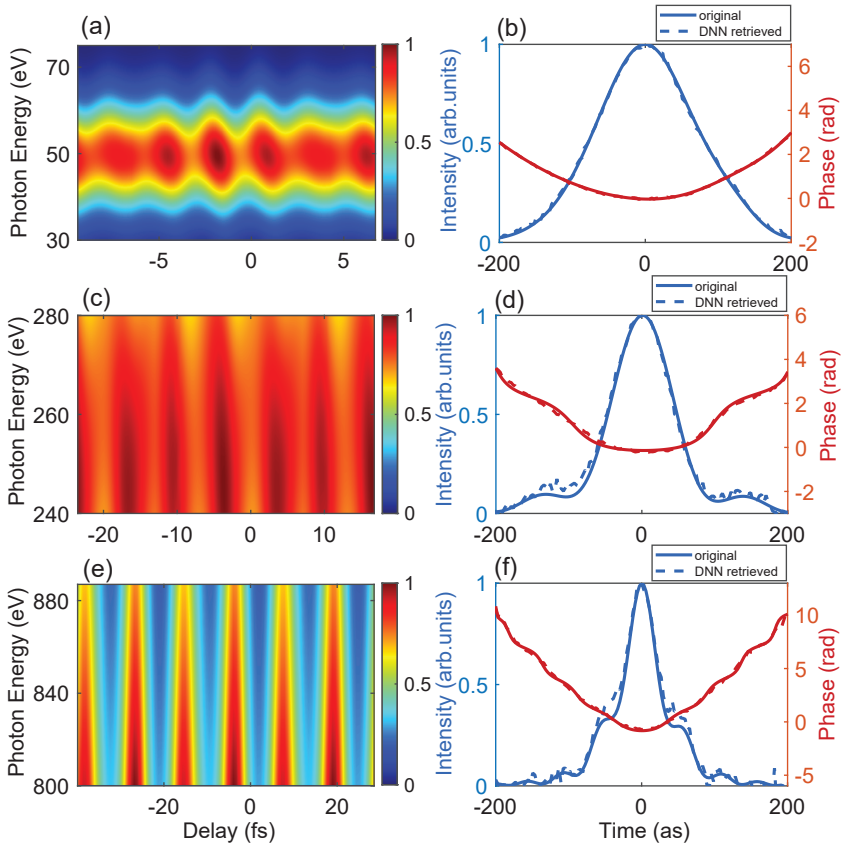

Fig. 6. Reconstruction of isolated attosecond pulses with the DNN model. (a), (c), and (e) Spectrograms as input to the DNN model, corresponding to Figs. 1(a), 2(a), and 2(d), respectively. (b), (d), and (f) Reconstruction of isolated attosecond pulses (dashed lines) from (a), (c), and (e), compared to the original pulses (solid lines).

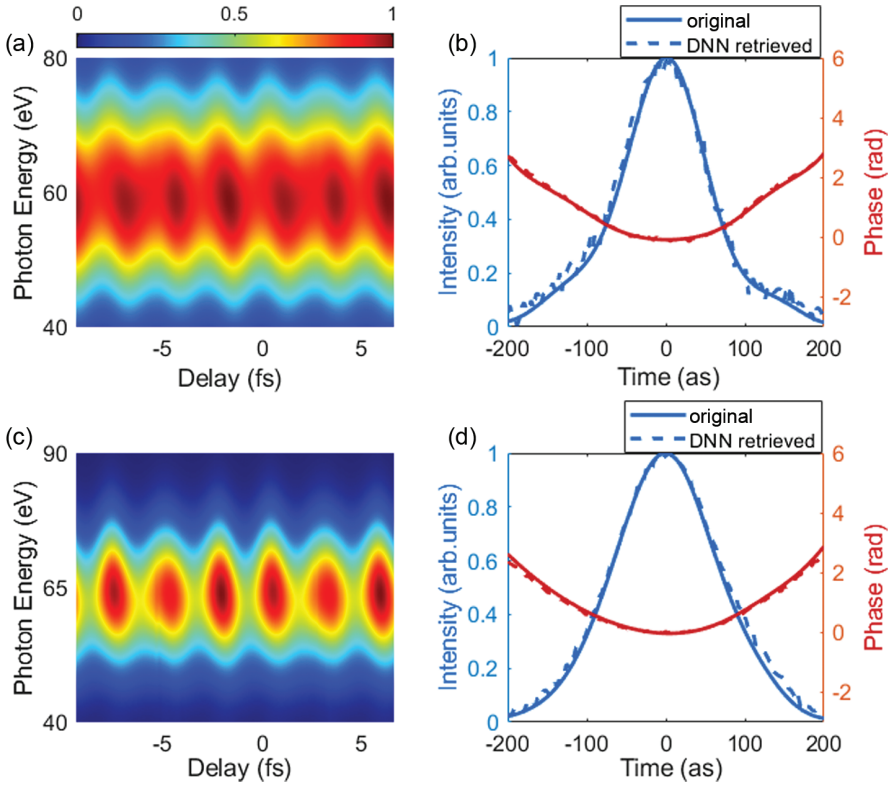

Fig. 7. DNN reconstruction of attosecond pulses generated by driving pulses centered at 800 nm. (a) and (c) Simulated spectrograms. (b) and (d) Reconstruction of attosecond pulses (dashed lines) from (a) and (c) compared to the original pulses (solid lines).

Next, we changed other generation parameters instead of the wavelength to test our model. The wavelength is fixed at 800 nm. In Fig. 7(a), we set the intensity of the driving pulse to 4×10^{14} W/cm^2 and selected the spectrogram bandwidth of 40 eV (40 eV to 80 eV). The duration of the generated pulse is 121 attoseconds. In Fig. 7(c), the gas target has changed from argon to neon, and the intensity is set to 3×10^{14} W/cm^2. The generated pulse duration is 154 attoseconds. As is shown in Figs. 7(b) and 7(d), both the amplitude and the phase of the retrieved pulses agree well with the original pulses.

The methods in [31,32] are also based on the neural network for attosecond characterization. Comparing our method to their methods was valuable. Their methods retrieve the spectral phase from the modulated photoelectron spectroscopy. The measurement of the photoelectron spectra always faces the space charge effect and therefore the efficiency of the data accumulation is low. Our method is based on the all-optical measurement scheme, which can overcome this problem and the data accumulation efficiency is much higher. Besides, the all-optical measurement technique could introduce less noise. On the other hand, we also compared the retrieved results between [31] and our method. In Figs. 7(b) and 7(d), the mean square error (MSE) values of the pulses are calculated as 0.0048 and 0.0093, respectively. Both of the MSE values are as low as those in [31]. Moreover, we have demonstrated that our method still has a good retrieval quality for the shorter pulse including sub-50 attoseconds pulse. These indicate that our method is a more convenient and reliable approach.

E. Robustness of the Deep Learning Method

To improve the robustness of our DNN model and make the simulations resemble the noisy conditions of the real experiment, we add noise to the spectrogram traces and mix them into the dataset to train the DNN model. We apply the SNR to quantify the noise level in the spectrogram traces. Here, the SNR is defined as

$$\mathrm{SNR} = 10 \log_{10} \left[\frac{\sum_x \sum_y S_{\mathrm{signal}}[x, y]}{\sum_x \sum_y S_{\mathrm{noise}}[x, y]} \right], \tag{7}$$

where S_{signal} is the spectrogram without noise and $S_{\mathrm{noise}}[x, y]$ is the noise in the spectrogram. We add the noise of SNR $\approx$ 3, 5, 7, 10, 15 to a spectrogram. The original spectrogram traces are shown in Figs. 8(a)–8(e). Figures 8(f)–8(j) present the retrieval results with the PCGPA. One can see that the PCGPA retrieved pulse shows disagreements with the original pulse when SNR $\approx$ 7. The reconstruction of the isolated attosecond pulse appears rather distorted when SNR $\approx$ 3. The retrieval results with the DNN model are shown in Figs. 8(k)–8(o). All of the retrieved pulses are nearly consistent with the original pulse, including the amplitude and the phase.

The spectra measured at different times would introduce different levels of noise. Therefore, more noise would be present along the time axis. This type of more time-dependent noise is common in laboratories. To test our model's robustness to such noises, we added different variances of the spectral noise as the delay changed. The spectrogram is shown in Fig. 9(a). We set

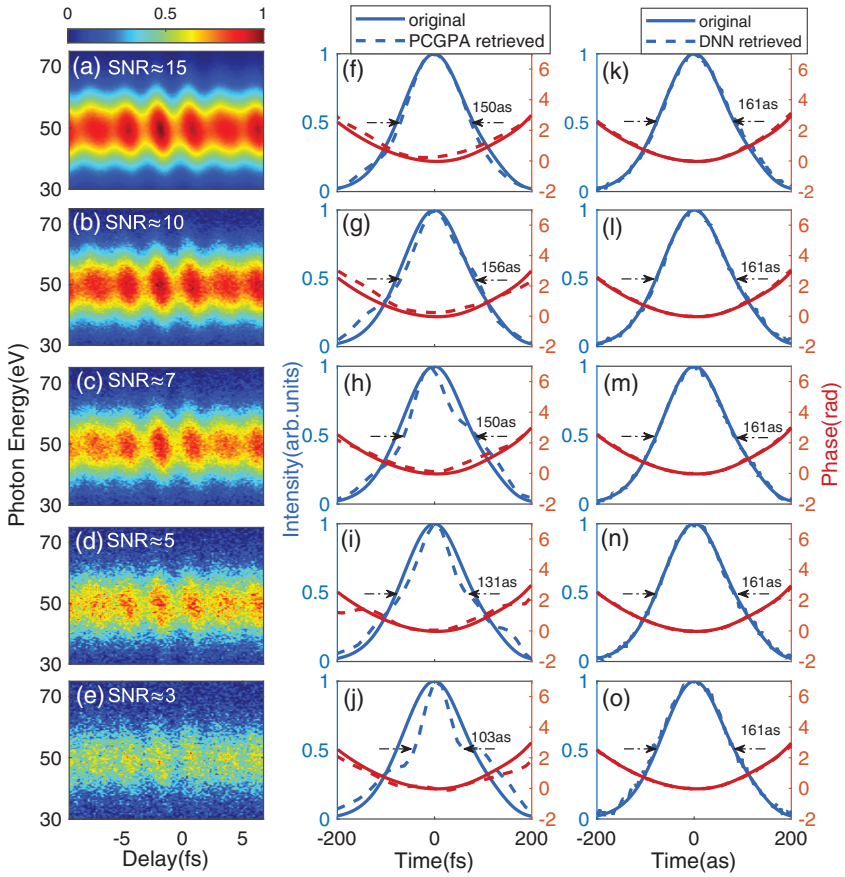

Fig. 8. Retrieval results from the spectrograms with the noise of different SNRs. (a)–(e) Spectrograms with the noise of SNR ≈ 3, 5, 7, 10, 15. (f)–(j) Retrieved pulses (dashed lines) from (a)–(e) with the PCGPA, compared to the original pulses (solid lines). (k)–(o) Retrieved pulses (dashed lines) from (a)–(e) with the DNN model, compared to the original pulses (solid lines).

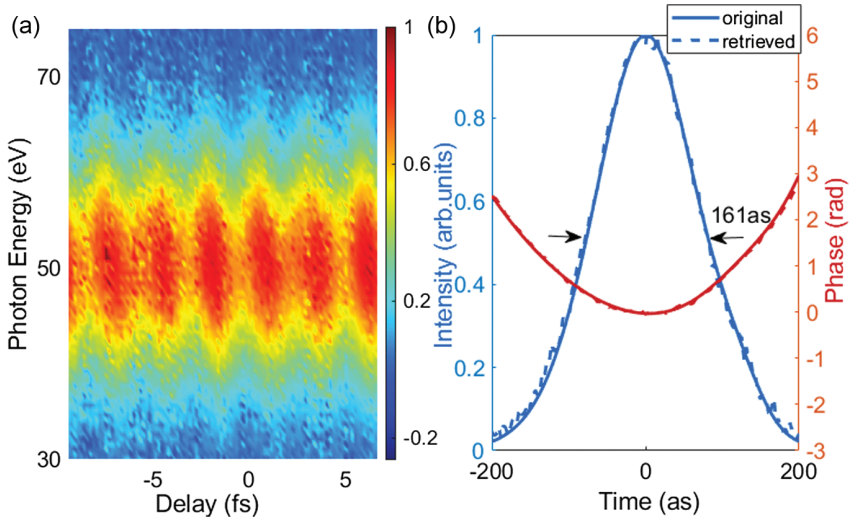

Fig. 9. Reconstruction results for testing robustness to more time-dependent noise. (a) Simulated spectrogram with noise. (b) Reconstruction of attosecond pulses (dashed lines), compared to the original pulse (solid lines).

SNR ≈ 7. As shown in Fig. 9(b), the retrieved amplitude and phase are consistent with the original pulse.

To evaluate the reconstruction ability of the DNN models, we qualified the performance for the pulse predictions. The error quality criterion is defined as

$$Q = \left[\frac{\sum_i w[i] * (y_I - \widetilde{y_I})^2}{\sum_i w[i]}\right]^{1/2} + \gamma * \left[\frac{\sum_i w[i] * (y_\Phi - \widetilde{y_\Phi})}{\sum_i w[i]}\right]^{1/2}. \quad (8)$$

Here, we set $\gamma = 0.05$. Figure 10 presents the performance of the different retrieval algorithms in the all-optical schemes.

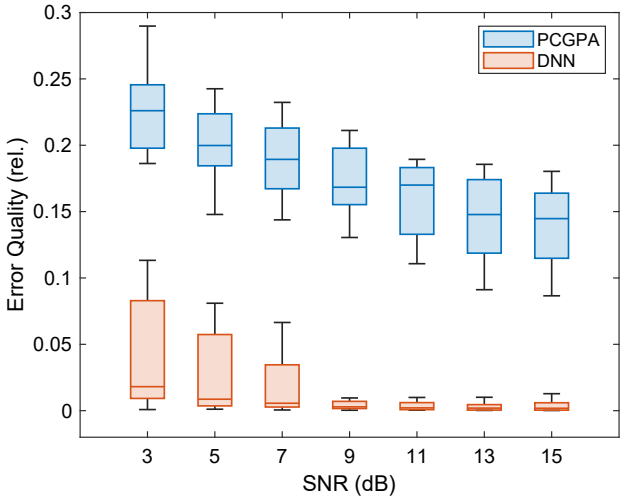

Fig. 10. Error quality as a function of the noise level. Box plots describe the error quality for different algorithms: the PCGP (blue) and the DNN model trained with noise (red). The lower value means a higher reconstruction quality.

When SNR ≤ 11, the PCGPA's error quality rapidly increases to more than 0.1. The error quality of the DNN reconstruction is still below 0.1 when SNR $= 3$. It's obvious that the error quality of the reconstruction with the DNN model is much lower than PCPG algorithm. When increasing the noise, the performance of the DNN model is much better than that of the PCGPA.

F. Retrieve the Sophisticated Temporal Profiles of Isolated Attosecond Pulse

The chirp with high-order dispersion can be sophisticated in HHG. For the ultrabroad spectrum, the attosecond pulse usually has a complicated shape in the time domain. It requires the algorithm to have abilities to retrieve the sophisticated temporal profile. To test this ability, we employ the few-cycle pulses centered at 2000 nm as the driving fields. The intensity of the driving field is 3×10^{14} W/cm^2. The perturbing pulse has the same wavelength, but the intensity is 1×10^{11} W/cm^2. Figure 11(a) presents the entire ultrabroad bandwidth spectrogram. As is shown in Figs. 11(b)–11(d), we select the spectrogram bandwidth of 40 eV (240 eV to 280 eV), 60 eV (240 eV to 300 eV) and 70 eV (230 eV to 300 eV), respectively. When the bandwidth is 40 eV, the retrieved pulses with both the PCGPA and the DNN model agree well with the original pulse, as shown in Figs. 11(e) and 11(h). When the bandwidth is increased to 60 eV, the central peak of the retrieved pulse with the PCGPA is the same as the original one, but the retrieved small side peaks show disagreements, as shown in Fig. 11(f). The duration of the original pulse is 128 attoseconds, and the retrieved pulse duration is only 73 attoseconds. In contrast, the DNN method can recover the details of the original pulse, including the central peak and the small side peaks, as shown in Fig. 11(f). When the spectrogram bandwidth is further increased to 70 eV, the original pulse has an obvious second peak. As shown in Fig. 11(g), the PCGPA can just retrieve the central peak, and the retrieved pulse duration is only about one-third of the original duration. The DNN method, however, still retrieves the shape of both the central peak and the second peak, as shown in Fig. 11(j). The duration of the DNN retrieved pulse is 188 attoseconds and agrees well with the original pulse duration.

3. CONCLUSION

We investigated isolated attosecond pulse reconstruction with the all-optical method. Our results show that the all-optical method enables diagnosis of the isolated attosecond pulses with a duration shorter than 100 attoseconds. However, it is difficult

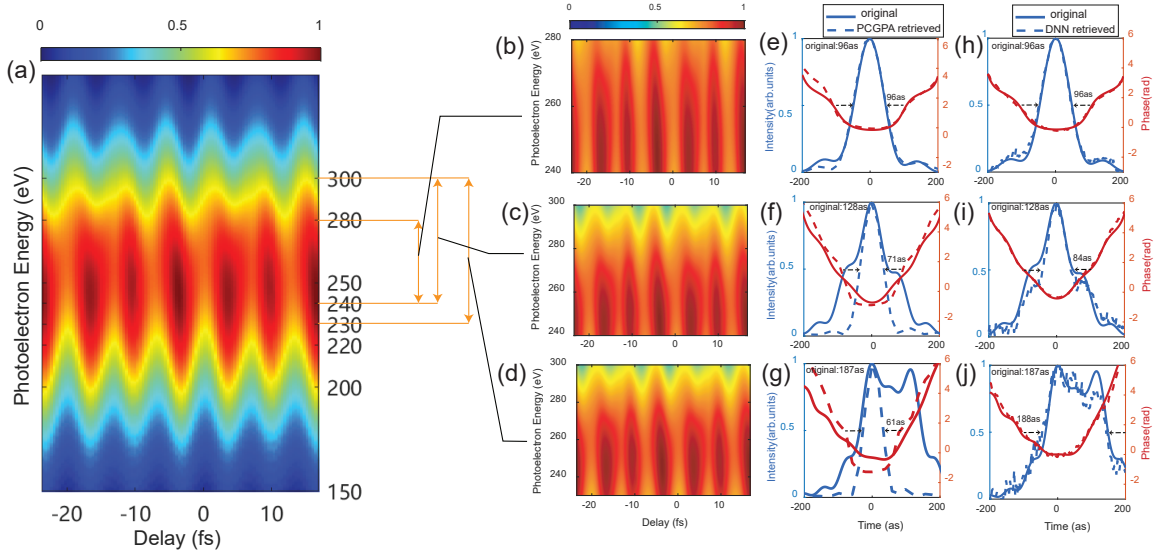

Fig. 11. Retrieval of the sophisticated temporal profiles with the PCGPA and the DNN model. (a) Entire ultrabroad spectrogram trace. (b)–(d) Spectrograms with different bandwidths: 40 eV, 60 eV, and 70 eV. (e)–(g) Reconstruction of attosecond pulses (dashed lines) with the PCGPA from (b)–(d), compared to the original pulses (solid lines). (h)–(j) Reconstruction of attosecond pulses (dashed lines) with the DNN model from (b)–(d), compared to the original pulses (solid lines).

to retrieve the sophisticated profile using the conventional PCPG algorithm, and the retrieval process is time-consuming. Therefore, we demonstrated a deep learning approach to reconstruct isolated attosecond pulses with the all-optical method. Our DNN method achieves the mapping from the spectrograms to isolated attosecond pulses via supervised learning. It has a superior retrieved quality compared to the PCGPA, especially at high noise levels. Our DNN method also is able to recover the sophisticated details of the pulse profile. Moreover, it spends only a few seconds on pulse reconstruction. We believe our approach provides a reliable and effective way to characterize isolated attosecond pulses.

Funding. National Natural Science Foundation of China (No. 12021004, No. 12074136, No. 12225406, No. 91950202).

Disclosures. The authors declare no conflicts of interest.

Data availability. Data underlying the results presented in this paper are not publicly available at this time but may be obtained from the authors upon reasonable request.

REFERENCES

1. P. M. Paul, E. S. Toma, P. Breger, G. Mullot, F. Augé, P. Balcou, H. G. Muller, and P. Agostini, "Observation of a train of attosecond pulses from high harmonic generation," Science **292**, 1689–1692 (2001).
2. M. Hentschel, R. Kienberger, C. Spielmann, G. A. Reider, N. Milosevic, T. Brabec, P. Corkum, U. Heinzmann, M. Drescher, and F. Krausz, "Attosecond metrology," Nature **414**, 509–513 (2001).
3. R. Kienberger, E. Goulielmakis, M. Uiberacker, A. Baltuska, V. Yakovlev, F. Bammer, A. Scrinzi, T. Westerwalbesloh, U. Kleineberg, U. Heinzmann, M. Drescher, and F. Krausz, "Atomic transient recorder," Nature **427**, 817–821 (2004).
4. E. Goulielmakis, Z.-H. Loh, A. Wirth, R. Santra, N. Rohringer, V. S. Yakovlev, S. Zherebtsov, T. Pfeifer, A. M. Azzeer, M. F. Kling, and S. R. Leone, "Real-time observation of valence electron motion," Nature **466**, 739–743 (2010).
5. H. J. Wörner, J. B. Bertrand, D. V. Kartashov, P. B. Corkum, and D. M. Villeneuve, "Following a chemical reaction using high-harmonic interferometry," Nature **466**, 604–607 (2010).
6. Z. Tao, C. Chen, T. Szilvási, M. Keller, M. Mavrikakis, H. Kapteyn, and M. Murnane, "Direct time-domain observation of attosecond final-state lifetimes in photoemission from solids," Science **353**, 62–67 (2016).
7. I. P. Christov, M. M. Murnane, and H. C. Kapteyn, "High-harmonic generation of attosecond pulses in the 'single-cycle' regime," Phys. Rev. Lett. **78**, 1251–1254 (1997).
8. T. Brabec and F. Krausz, "Intense few-cycle laser fields: frontiers of nonlinear optics," Rev. Mod. Phys. **72**, 545–591 (2000).
9. P. B. Corkum, N. H. Burnett, and M. Y. Ivanov, "Subfemtosecond pulses," Opt. Lett. **19**, 1870–1872 (1994).
10. C. Altucci, C. Delfin, L. Roos, M. B. Gaarde, A. L'Huillier, I. Mercer, T. Starczewski, and C.-G. Wahlström, "Frequency-resolved time-gated high-order harmonics," Phys. Rev. A **58**, 3934–3941 (1998).
11. G. Sansone, E. Benedetti, F. Calegari, C. Vozzi, L. Avaldi, R. Flammini, L. Poletto, P. Villoresi, C. Altucci, R. Velotta, S. Stagira, S. D. Silvestri, and M. Nisoli, "Isolated single-cycle attosecond pulses," Science **314**, 443–446 (2006).
12. Z. Chang, "Controlling attosecond pulse generation with a double optical gating," Phys. Rev. A **76**, 051403 (2007).
13. T. Pfeifer, L. Gallmann, M. J. Abel, D. M. Neumark, and S. R. Leone, "Single attosecond pulse generation in the multicycle-driver regime by adding a weak second-harmonic field," Opt. Lett. **31**, 975–977 (2006).
14. Y. Oishi, M. Kaku, A. Suda, F. Kannari, and K. Midorikawa, "Generation of extreme ultraviolet continuum radiation driven by a sub-10-fs two-color field," Opt. Express **14**, 7230–7237 (2006).
15. H. Merdji, T. Auguste, W. Boutu, J.-P. Caumes, B. Carré, T. Pfeifer, A. Jullien, D. M. Neumark, and S. R. Leone, "Isolated attosecond pulses using a detuned second-harmonic field," Opt. Lett. **32**, 3134–3136 (2007).
16. P. Lan, P. Lu, Q. Li, F. Li, W. Hong, and Q. Zhang, "Macroscopic effects for quantum control of broadband isolated attosecond pulse generation with a two-color field," Phys. Rev. A **79**, 043413 (2009).
17. J. Li, X. Ren, Y. Yin, K. Zhao, A. Chew, Y. Cheng, E. Cunningham, Y. Wang, S. Hu, Y. Wu, M. Chini, and Z. Chang, "53-attosecond X-ray pulses reach the carbon K-edge," Nat. Commun. **8**, 186 (2017).
18. T. Gaumnitz, A. Jain, Y. Pertot, M. Huppert, I. Jordan, F. Ardana-Lamas, and H. J. Wörner, "Streaking of 43-attosecond soft-X-ray pulses generated by a passively CEP-stable mid-infrared driver," Opt. Express **25**, 27506–27518 (2017).
19. K. T. Kim, D. Villeneuve, and P. Corkum, "Manipulating quantum paths for novel attosecond measurement methods," Nat. Photonics **8**, 187–194 (2014).
20. Y. Mairesse and F. Quéré, "Frequency-resolved optical gating for complete reconstruction of attosecond bursts," Phys. Rev. A **71**, 011401 (2005).
21. N. Dudovich, O. Smirnova, J. Levesque, Y. Mairesse, M. Y. Ivanov, D. Villeneuve, and P. B. Corkum, "Measuring and controlling the birth of attosecond XUV pulses," Nat. Phys. **2**, 781–786 (2006).
22. K. T. Kim, C. Zhang, A. D. Shiner, S. E. Kirkwood, E. Frumker, G. Gariepy, A. Naumov, D. Villeneuve, and P. Corkum, "Manipulation of quantum paths for space–time characterization of attosecond pulses," Nat. Phys. **9**, 159–163 (2013).
23. Z. Yang, W. Cao, X. Chen, J. Zhang, Y. Mo, H. Xu, K. Mi, Q. Zhang, P. Lan, and P. Lu, "All-optical frequency-resolved optical gating for isolated attosecond pulse reconstruction," Opt. Lett. **45**, 567–570 (2020).
24. L. Chopineau, A. Denoeud, A. Leblanc, E. Porat, P. Martin, H. Vincenti, and F. Quéré, "Spatio-temporal characterization of attosecond pulses from plasma mirrors," Nat. Phys. **17**, 968–973 (2021).
25. L. He, J. Hu, S. Sun, Y. He, Y. Deng, P. Lan, and P. Lu, "All-optical spatio-temporal metrology for isolated attosecond pulses," J. Phys. B **55**, 205601 (2022).
26. D. Kane, "Recent progress toward real-time measurement of ultrashort laser pulses," IEEE J. Quantum Electron. **35**, 421–431 (1999).
27. J. Gagnon, E. Goulielmakis, and V. S. Yakovlev, "The accurate frog characterization of attosecond pulses from streaking measurements," Appl. Phys. B **92**, 25–32 (2008).
28. M. Lucchini, M. Brügmann, A. Ludwig, L. Gallmann, U. Keller, and T. Feurer, "Ptychographic reconstruction of attosecond pulses," Opt. Express **23**, 29502–29513 (2015).
29. T. Zahavy, A. Dikopoltsev, D. Moss, G. I. Haham, O. Cohen, S. Mannor, and M. Segev, "Deep learning reconstruction of ultrashort pulses," Optica **5**, 666–673 (2018).
30. S. Kleinert, A. Tajalli, T. Nagy, and U. Morgner, "Rapid phase retrieval of ultrashort pulses from dispersion scan traces using deep neural networks," Opt. Lett. **44**, 979–982 (2019).
31. J. White and Z. Chang, "Attosecond streaking phase retrieval with neural network," Opt. Express **27**, 4799–4807 (2019).
32. C. Brunner, A. Duensing, C. Schröder, M. Mittermair, V. Golkov, M. Pollanka, D. Cremers, and R. Kienberger, "Deep learning in attosecond metrology," Opt. Express **30**, 15669–15684 (2022).
33. M. Lewenstein, P. Balcou, M. Y. Ivanov, A. L'Huillier, and P. B. Corkum, "Theory of high-harmonic generation by low-frequency laser fields," Phys. Rev. A **49**, 2117–2132 (1994).
34. P. Lan, P. Lu, W. Cao, Y. Li, and X. Wang, "Isolated sub-100-as pulse generation via controlling electron dynamics," Phys. Rev. A **76**, 011402 (2007).
35. Y. D. Hezaveh, L. P. Levasseur, and P. J. Marshall, "Fast automated analysis of strong gravitational lenses with convolutional neural networks," Nature **548**, 555–557 (2017).
36. G. Huang, Z. Liu, L. Van Der Maaten, and K. Q. Weinberger, "Densely connected convolutional networks," in *IEEE Conference on Computer Vision and Pattern Recognition (CVPR)* (2017), pp. 2261–2269.

37. C. Szegedy, W. Liu, Y. Jia, P. Sermanet, S. Reed, D. Anguelov, D. Erhan, V. Vanhoucke, and A. Rabinovich, "Going deeper with convolutions," in *IEEE Conference on Computer Vision and Pattern Recognition (CVPR)* (2015), pp. 1–9.

38. F. Chollet, "Xception: deep learning with depthwise separable convolutions," in *IEEE Conference on Computer Vision and Pattern Recognition (CVPR)* (2017), pp. 1800–1807.